Marine Atmospheric Boundary Layer Divergence and Clouds along California in June 1996

DARKO KORAČIN

Desert Research Institute, Reno, Nevada

CLIVE E. DORMAN

Scripps Institution of Oceanography, La Jolla, California, and San Diego State University, San Diego, California

(Manuscript received 10 November 1999, in final form 13 December 2000)

ABSTRACT

The authors have performed a numerical experiment using Mesoscale Model 5 (MM5) with a horizontal resolution of 9 km to simulate hourly atmospheric dynamics and thermodynamics along the U.S. California coast for all of June 1996. The MM5 results were evaluated using more than 18 000 data points from wind profilers, radiosondes, buoys, and land stations; the results support the use of modeled dynamics for reliable monthly statistics and calculation of diurnal variations. Month-long mesoscale simulations of the marine atmospheric boundary layer (MABL) and satellite observations have been used to investigate the diurnal variation of near-shore and farther offshore clouds along the U.S. California coast. The authors extended the usual model evaluation with respect to time series and power spectrum analysis to investigate a link between the evaluated dynamics and satellite-derived cloudiness. Two distinct types of cloudiness variation were revealed. One is in the near-shore zone, extending approximately 100 km in the offshore direction, where the diurnal variation of cloudiness develops in response to the formation of MABL wind divergence and convergence fields. Each of the five major capes between southern Oregon and southern California has a satellite-derived, low-cloud maximum albedo on the leeward side and a minimum on the windward side that closely corresponds to ''expansion fans'' and ''compression bulges.'' The expansion fan is associated with a divergence field of fast horizontal winds, shallow MABL, and high Froude number. The compression bulge is associated mainly with relatively weak winds (convergent or slightly divergent), a deeper MABL, and smaller Froude number. Simulated divergence in the expansion fan areas shows a significant diurnal trend with the maximum during the late morning through early afternoon. In the compression bulge, either the divergence is an order of magnitude less, or the flow becomes convergent. Going westward, the MABL divergence becomes an order of magnitude less at distances of 30–40 km from the coastline. Since the expansion fan is characteristic of the MABL, the effect of the divergence field decays rapidly in the vertical and, due to mass continuity, reverses into a convergent flow above the MABL.

Farther offshore, the cloudiness variation is at a minimum around midday as well, but that is mainly a consequence of radiative heat transfer effects within the cloud. Marine atmospheric boundary layer divergence does not have a significant diurnal trend in that area. Daytime offshore cloud clearing begins first in the northern domain, where the marine layer and clouds are shallower. The clearing propagates southward until the marine layer and clouds are too deep; generally the clouds persist throughout the entire day.

The study shows the importance of dynamics on the evolution of observed cloudiness and constitutes an approach to indirectly evaluate modeled dynamics using satellite-derived cloudiness.

1. Introduction

The summer sea level wind field along the U.S. West Coast is important to a range of scientific interests, including the response of the coastal ocean and its biology to the alongshore component of wind stress, the wind stress divergence, and the wind stress curl. The wind field is also important to operational interests such as fishing vessels, small craft, and aviation. Direct measurements of the surface winds are limited to a modest number of near-coast buoys separated by distances of 100–200 km. These and the few applicable land stations are inadequate to resolve the horizontal structure or diurnal variations of the surface winds. This has come to light through a series of field programs and theoretical development that forced a change in the view of the marine atmospheric boundary layer (MABL).

The focus of earlier analyses was restricted to the large-scale structure of atmospheric conditions. Ship-based climatologies showed the broadest details, with a summer wind speed maximum along southern Oregon and northern California (Nelson 1977; Nelson and Husby 1983). Automated coastal buoys in the 1980s pro-

Corresponding author address: Dr. Darko Koračin, Desert Research Institute, 2215 Raggio Parkway, Reno, NV 89512.
E-mail: darko@dri.edu

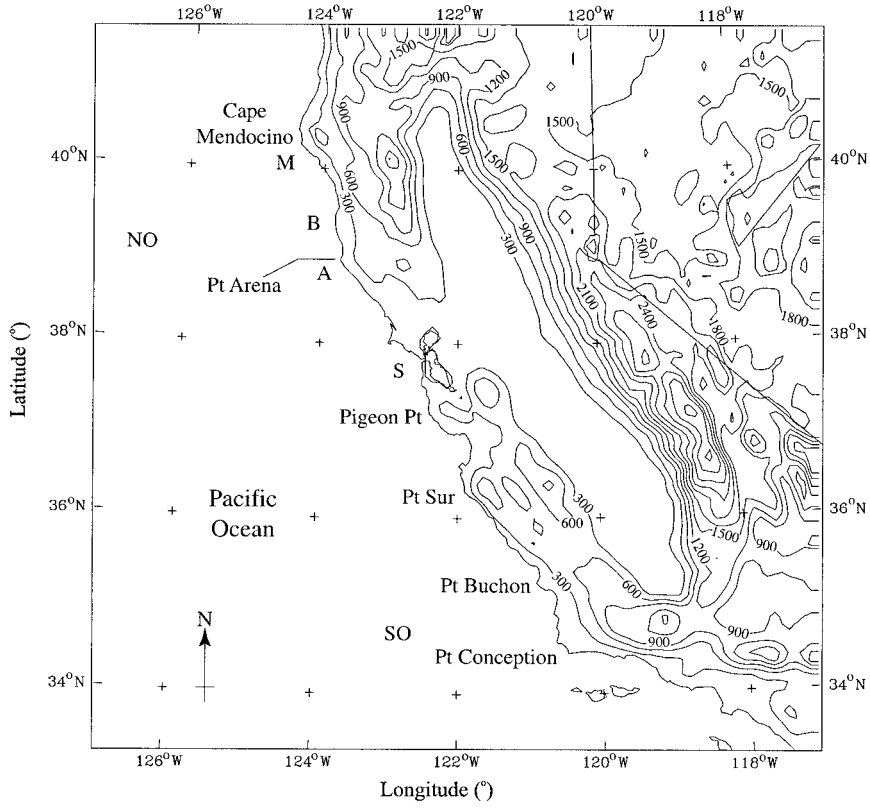

FIG. 1. Map of the model domain and topography. Characters mark locations where diurnal trends are referred to later.

vided the first over-water data at about a dozen locations, which showed that there were two summer west coast wind speed peaks, and also provided information on the synoptic and diurnal variations of wind conditions at a limited number of locations (Dorman and Winant 1995). Over time, it became apparent that the three-dimensional nature of the MABL was related to the wind field. Using limited observations, Neiburger et al. (1961) inferred that the air temperature inversion base that caps the marine layer is low near the California coast and rises offshore. Measurement of the complexity of the coastal winds and MABL structure down to a 1-km scale occurred in the early 1980s with daytime aircraft flights, buoys, and coastal soundings in a 100-km section between Bodega Bay and Point Arena, California (Beardsley et al. 1987). A conceptual model of the typical diurnal trend of the winds and MABL depth in the cross-shore direction was constructed based upon surface station measurements and coastal radiosoundings. The discovery that the MABL flow was supercritical provided a dynamically based explanation for the significant variation in the surface winds and MABL depth (Dorman 1985; Winant et al. 1988). Supercriticality occurs when the Froude number (Fr) is greater than 1.0 and also provides the dynamic link between the surface winds and the MABL depth.

While investigating the west coast MABL conditions, modelers were able to examine the ramifications of supercriticality on the coastal flow (Samelson 1992; Burk and Thompson 1996; Rogers et al. 1998; Tjernström 1999; Tjernström and Grisogono 2000). Approaching a cape, a supercritical marine layer will slow and thicken, forming what we shall refer to as a ''compression bulge'' on the upwind side. As the supercritical marine flow passes the end of the cape, it accelerates and the marine layer thins forming a shallow layer associated with a wind speed maximum called an ''expansion fan.'' The horizontal area for expansion fans and compression bulges is on the order of 10 km. A study by Rogerson (1999) showed that an expansion fan would occur if the approaching marine layer flow is transcritical ($0.5 < \text{Fr} < 1.0$). Farther downwind of an expansion fan, if the flow does not encounter another topographically forced feature, the marine layer will slow in the zone that we shall refer to as a ''decelaration area.''

The supercriticality of the west coast summer marine layer and the existence of these topographically forced features have been confirmed by aircraft and modeling studies. Aircraft have mapped compression bulges upwind and supercritical expansion fans downwind of Cape Blanco (Oregon Coast), Cape Mendocino, Point Arena, and Point Sur (Winant et al. 1988; Rogers et al. 1998; Dorman et al. 1999); see Fig. 1 for the locations of the topographical points. Furthermore, aircraft ob-

servations show a compression bulge upwind of Point Conception while surface observations and coastal soundings indicate that a transcritical expansion fan forms in the lee of Point Conception (Dorman and Winant 2000). The existence of supercritical marine layer conditions from southern Oregon to Point Conception, California, and extending more than 100 km offshore has been supported by regional-scale models (Rogers et al. 1998; Dorman et al. 2000). The importance and interplay between the cloudiness and dynamics over the California coastal waters was discussed by Koračin and Tjernström (1992) and over the Baltic Sea by Sundararajan and Tjernström (2000).

It appears that the mean conditions and the generalized structure of the marine layer can be explained, but several aspects are still missing. Most previous modeling studies were limited to idealized conditions or were of short duration. The mean horizontal extent of topographically forced MABL features and their offshore extent have not been resolved by the few aircraft flights. The divergence of the wind field has not been resolved by buoys and, until recently, was not resolved by regional-scale models either. And neither buoys, aircraft, nor models were able to shed light on the alongcoast offshore extent and the diurnal variation of topographically forced MABL features.

Since simulation of cloudiness always has uncertainties and errors due to the initial and boundary conditions, parameterization of water phase changes, model grid resolution, and even methods of comparison with measurements, we focus on the more reliable simulated dynamics (evaluated using measurements) and processed satellite data. The main objective is to show the importance of coastal dynamics on the evolution of observed cloudiness. The approach, in short, is comprehensive evaluation of model dynamics using satellite data.

The main objective of this study is to investigate the diurnal variability of MABL dynamics and cloudiness off the California and Oregon coasts for all of June 1996. Hourly results from month-long simulations using Mesocale Model 5 (MM5; Grell et al. 1995) are used to infer the diurnal variability of winds, the divergence field, and MABL properties and their impact on the evolution of coastal cloudiness. Diurnal variability of cloud albedo determined from satellite data is then compared to the diurnal variability of the simulated flow divergence.

2. Method

For the purpose of investigating causality between the properties and the diurnal variation of the coastal marine flow and cloudiness, we used month-long mesoscale simulations from the MM5 model and stationary satellite observations of cloud albedo for all of June 1996.

a. Model setup

The MM5 model is a community model developed jointly by the Pennsylvania State University and the National Center for Atmospheric Research in Boulder, Colorado. It is used worldwide, and details can be found on the World Wide Web site http://www.mmm.ucar.edu/mm5. Detailed information on the structure and optional parameters of the MM5 code is provided by Grell et al. (1995).

For this study, a model grid of 101 $\times$ 101 horizontal points, centered at 37.5°N, 122.0°W, was used. The grid covered a 900 km $\times$ 900 km area (Fig. 1) with a horizontal resolution of 9 km. The MM5 model in a nonhydrostatic mode was used for all simulations. The model grid consists of 35 points in vertical sigma coordinates, providing a resolution of approximately 40 m in the first several hundred meters above the surface, expanding toward the top of the model domain. Topography for the simulation was based on a 5-min resolution global terrain dataset, and land use was based on a 10-min resolution dataset. First-guess synoptic fields (for every 12 h and 10 standard pressure levels) as well as sea surface temperature distribution were obtained from the U.S. National Centers for Environmental Prediction archive of global analysis. The synoptic inputs include virtual temperature, geopotential height, U and V wind components, and relative humidity. This synoptic information is horizontally interpolated into the model grid by a two-dimensional, 16-point overlapping parabolic fit. Assimilation of all available upper-air and surface stations into the synoptic fields was performed by objective analysis. The MM5 model was run with a simple moisture scheme and included a parameterization of shortwave and longwave radiative effects. A full Coriolis 3D option, radiative condition at the upper boundary, and relaxation options were used in this simulation. We used the Blackadar (1979) planetary boundary layer scheme and the Grell et al. (1995) cumulus parameterization. In this simulation, surface heat and moisture fluxes over the land were computed and ground temperature was predicted. The integration time step was 27 s, and the model results were stored at hourly intervals for all of June 1996. The raw output files were then processed to obtain daily averaged files. Each daily average file contained wind components, temperature, and humidity for all points of the 3D domain. Several sensitivity tests relating to horizontal and vertical resolutions as well as the range of the domain were made to optimize the model setup for the relatively long-term mesoscale simulations. The model domain and topography are shown in Fig. 1.

b. Model evaluation

There are more than 200 peer-reviewed publications (see the above mentioned World Wide Web site) that focus on MM5 model development, applications, and

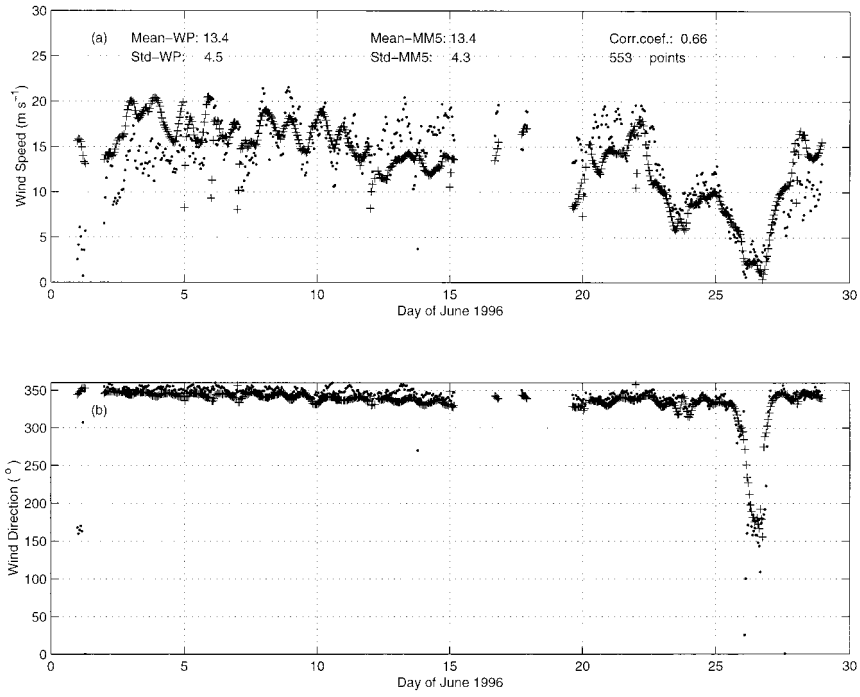

FIG. 2. Time series of radar wind profiler data (·) and MM5 modeled (+) (a) wind speed and (b) wind direction at 300 m AGL at Point Arena for all of Jun 1996.

various levels of evaluation. Most California coastal studies have focused on events of short duration, however, and placed little emphasis on model evaluation. Therefore, we performed a preliminary evaluation of the MM5 model results for all of June 1996 (Koračin et al. 1997, 1998). Data were obtained from coastal wind profilers, buoys, radiosondes, and aircraft measurements conducted during the Coastal Waves'96 Experiment described in Rogers et al. (1998).

Here we present the model evaluation results and illustrate the behavior of coastal dynamics over the month-long period. Two typical comparisons of simulated and observed profiler winds at Point Arena are shown for 300 (Fig. 2) and 1500 m (Fig. 3) above ground level (AGL). From the surface to 1000 m, strong winds were both simulated and measured during the entire month. Both measured and simulated monthly average wind speeds at 300 m AGL were in excess of 13 m s^{-1}, with similar variability and a close correlation overall. The monthly averaged simulated and measured wind speeds above the MABL (at 1500 m AGL) were much lower (8.5 and 6.9 m s^{-1}, respectively) compared to the MABL wind speeds.

Basic statistical parameters for the MM5 evaluation using the data from three wind profilers, nine buoys, and two land (shoreline) stations are shown in Table 1. Correlation coefficients between the simulated and measured wind speed and direction were generally from 0.5 to 0.7 and 0.7 to 0.9, respectively. The parameters in the table are defined as follows.

- The bias or mean error (me):

$$\text{bias} = \text{me} = \frac{1}{n}\sum_{i=1}^{n}(S_i - O_i) \tag{1}$$

- The mean absolute error (mae):

$$\text{mae} = \frac{1}{n}\sum_{i=1}^{n}|S_i - O_i| \tag{2}$$

- The population root-mean-square error (rmse):

$$\text{rmse} = \sqrt{\frac{1}{n}\sum_{i=1}^{n}(S_i - O_i)^2} \tag{3}$$

- The root-mean-square vector error (rmsve):

$$\text{rmsve} = \sqrt{\frac{1}{n}\sum_{i=1}^{n}[(U_{si} - U_{oi})^2 + (V_{si} - V_{oi})^2]} \tag{4}$$

where n is the number of points for comparison, S represents the wind speed simulated by the MM5 model, O represents the corresponding observed value, U_s and V_s are the wind speed components simulated by the MM5 model, and U_o and V_o are the observed wind components in the x and y directions, respectively. Mean error is generally low for wind profiler data. The low correlation coefficient for wind profiler data at the lowest measuring level may be explained by less reliable measurements near the vertical threshold. The number of measured samples at the lowest measuring level was much smaller than at other levels.

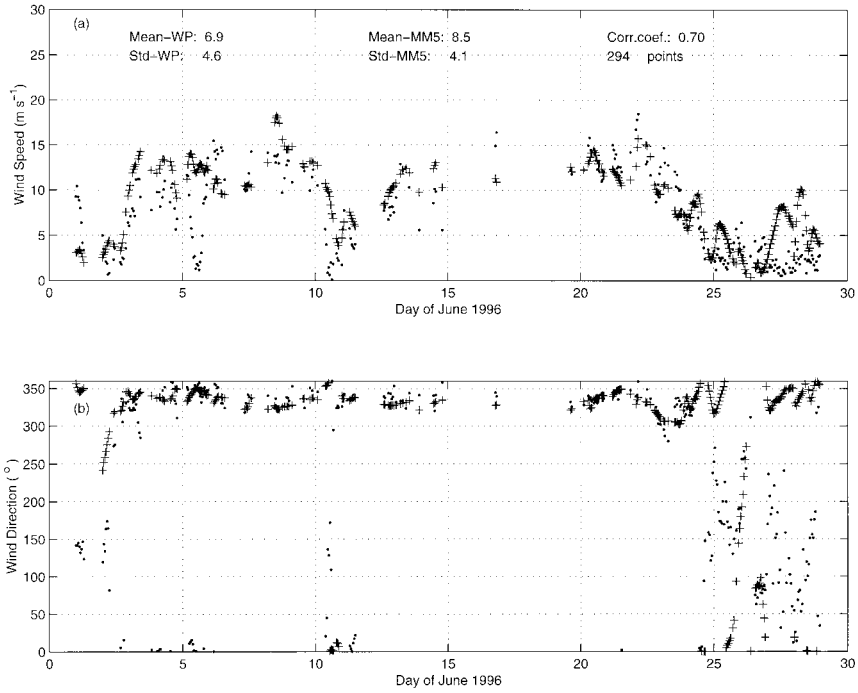

FIG. 3. Time series of radar wind profiler data (·) and MM5 modeled (+) (a) wind speed and (b) wind direction at 1500 m AGL at Point Arena for all of Jun 1996.

The relatively high mean error for the buoy is a consequence of the differences in vertical levels between the model output and measurements. The modeled averages are greater than the measured ones since the buoy sensor heights are lower than the first model vertical level. This is further explained using the comparison between the model results and data from buoy 46042 located near Monterey Bay. As can be expected, the simulated wind at 20 m is usually faster than the measured wind at 5 m. The average ratio between the simulated and measured wind speed is 1.24. Assuming that the average wind speed can be simply expressed with a logarithmic function for neutral stability conditions and choosing a roughness length of 0.05 m, the expected ratio between the simulated and measured wind speeds at these two different levels is in a similar range (1.31).

The mae, rmse, and rmsve indicate that there are occasionally noticeable differences between the model results and observations. A close inspection of the time series of wind profiler data (Figs. 2, 3) shows that there were some outliers in measurements occurring either before or after a period of missing data. When comparing large model and measurements data sets (over 18 000 points), including some measured data of questionable quality is generally unavoidable. A close inspection of the cases with low correlation, such as Piedras Blancas at 1000 m AGL, shows frequent drops in wind speed (almost to zero), possibly due to some instrument problems, that are not seen at these levels in other wind profiler data (figure not shown). Note that all normalized error parameter values for Point Arena are relatively low since the averages are quite high.

Our primary interest is to use the simulation results to infer average dynamics properties for all of June 1996. Similar basic statistical parameters between the simulations and measurements, as well as similar temporal patterns in both wind speed and direction, indicate that the simulation results can be used for that purpose.

A spectral analysis of the hourly observed and simulated wind speeds revealed that the model was able to reproduce the diurnal periodicity present in both buoy and wind profiler data. Figure 4 shows power spectra versus period for the hourly wind speed measured at 300 m by a wind profiler at Fort Ord and simulated by the MM5 model. The figure confirms that the model was able to simulate the diurnal periodicity in the wind speed at the coastal profiler. Figure 5 shows power spectra versus period for the hourly wind speed measured at buoy 46042 (off Monterey Bay). Both the measurements and model indicate that diurnal variation is present at that location.

In summary, on the basis of more than 18 000 simultaneous points of comparison between the simulated and measured wind speed, we conclude that MM5 results compare favorably with the wind profiler and buoy data. The close agreement between the model and measurements gives us confidence in analyzing MM5 results throughout the entire domain in order to understand the dynamics over both the coastal waters and offshore regions.

TABLE 1. Basic statistics of the MM5 model evalutation for wind speed (m s^{-1}) using the wind profiler, buoy, and land (shoreline) stations for all of June 1996. Annotations with wind profiler heights ''L'' and ''H'' indicate the wind measurements in low and high vertical resolution modes, respectively.

Location*	N Lat	W Long	Height (m) MSL	*N*	Mean MM5	Mean OBS	Std dev MM5	Std dev OBS	Corr	Me	Mae	Rmse	Rmsve
BBY	38.19	123.03											
			200	649	10.5	9.0	2.7	6.1	0.39	1.46	4.77	5.79	7.22
			300	647	11.0	9.0	3.0	6.1	0.41	1.92	4.74	5.92	7.20
			1000	620	9.0	6.7	4.1	4.4	0.59	2.34	3.64	4.51	5.45
			1500 H	464	6.2	6.1	3.1	3.3	0.52	0.15	2.47	3.13	4.95
			1500 L	564	6.5	6.3	3.1	3.3	0.54	0.17	2.45	3.07	4.89
FTO	36.41	121.46											
			200	338	4.6	5.0	2.4	2.4	0.41	−0.32	2.03	2.60	4.23
			300	704	4.8	5.5	2.3	2.6	0.63	−0.64	1.75	2.20	4.50
			1000	619	6.9	5.4	2.7	2.6	0.61	1.47	2.14	2.74	4.13
			1500 H	400	5.7	4.7	2.6	2.4	0.65	0.94	1.78	2.30	4.56
			1500 L	706	6.2	5.0	2.6	2.5	0.61	1.20	2.00	2.56	4.46
PAA	38.57	123.44											
			200	534	11.9	13.5	3.6	4.3	0.74	−1.58	2.65	3.33	4.17
			300	545	13.4	13.5	4.3	4.3	0.70	−0.12	2.68	3.35	4.00
			1000	485	11.5	10.2	3.8	4.7	0.69	1.26	2.85	3.68	4.26
			1500 H	286	8.6	6.9	4.1	4.7	0.72	1.75	2.94	3.76	5.34
			1500 L	396	8.5	7.3	4.2	4.7	0.71	1.23	2.85	3.60	5.06
PPB	35.4	121.17											
			200	672	11.1	6.5	4.2	4.7	0.54	4.69	5.37	6.35	9.26
			300	665	10.5	6.1	4.2	4.6	0.58	4.45	4.95	6.00	8.36
			1000	631	7.5	4.5	2.8	2.7	0.27	3.03	3.69	4.50	5.93
			1500 H	548	6.4	4.1	2.3	2.1	0.40	2.28	2.74	3.34	4.87
			1500 L	607	6.4	4.0	2.3	2.1	0.39	2.31	2.75	3.37	4.88
Buoys:													
46011	34.88	120.87	5 vs 20	700	9.3	5.9	2.8	3.0	0.73	3.46	3.51	4.07	4.46
46012	37.39	122.73	5 vs 20	706	9.1	6.0	2.7	1.9	0.61	3.16	3.24	3.81	4.06
46013	38.23	123.30	5 vs 20	703	11.9	10.3	3.1	3.3	0.60	1.60	2.63	3.28	4.03
46014	39.22	123.97	5 vs 20	699	9.5	7.8	3.0	3.6	0.67	1.66	2.56	3.17	3.69
46023	34.71	120.97	10 vs 20	330	10.1	10.0	2.9	3.1	0.71	0.10	1.69	2.30	2.87
46026	37.75	122.82	5 vs 20	696	10.6	7.0	2.8	2.5	0.53	3.53	3.71	4.39	4.72
46028	35.74	121.88	5 vs 20	701	10.1	8.9	2.7	3.3	0.74	1.18	2.02	2.49	3.77
46042	36.75	122.42	5 vs 20	707	8.4	6.8	2.5	2.1	0.66	1.57	1.99	2.48	2.83
46054	34.27	120.45	10 vs 20	704	10.9	9.3	3.0	4.3	0.66	1.62	2.69	3.60	4.68
PTAC1	38.96	123.74	29.9 vs 20	698	9.2	6.9	2.7	2.1	0.65	2.24	2.61	3.08	4.13
PTGC1	34.58	120.65	41.7 vs 20	702	9.5	8.6	2.8	3.9	0.62	0.87	2.55	3.24	6.12

* BBY, Bodega Bay; FTO, Fort Ord; PAA, Point Arena; PPB, Pierdras Blancas.

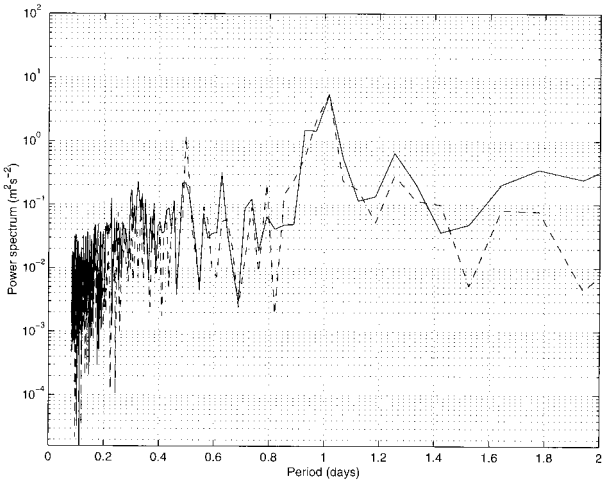

FIG. 4. Power spectra vs period for measured (wind profiler, solid line) and simulated (MM5 model, dashed line) hourly wind speed at Fort Ord at 300 m AGL for all of Jun 1996.

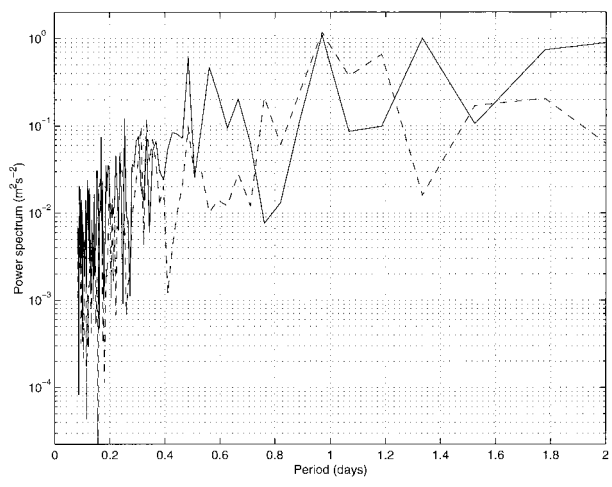

FIG. 5. Power spectra vs period for measured at 5 m (solid line) and simulated at 20 m AGL (dashed line) hourly wind speed at buoy 46042 (off Monterey Bay) for all of Jun 1996.

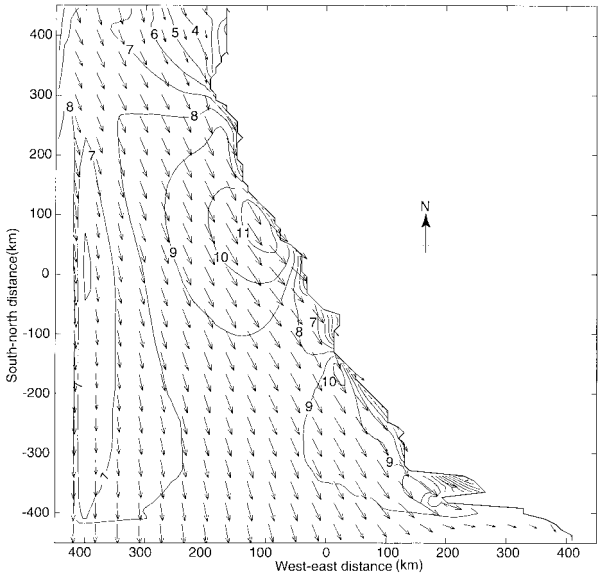

FIG. 6. Simulated wind vectors and contours of wind speed at 20 m AGL averaged for 0200 LST for all of Jun 1996. Contour interval for wind speed is 1 m s^{-1}.

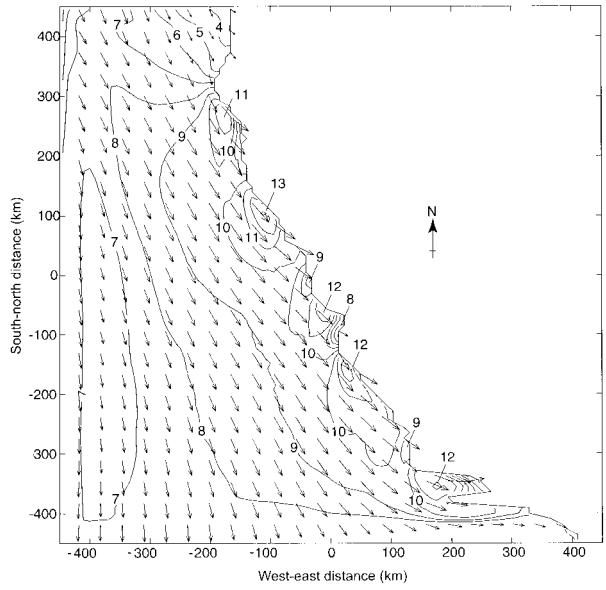

FIG. 7. Simulated wind vectors and contours of wind speed at 20 m AGL averaged for 1400 LST for all of Jun 1996. Contour interval for wind speed is 1 m s^{-1}.

c. Satellite observations

The Geostationary Operational Environmental Satellite *GOES-9* images for all of June 1996 were used for cloud observations. Cloud albedo was derived either from channel 1 or from the visible band images that were corrected for solar angle. Clouds with infrared temperatures (channel 4) more than 6 K colder than the most recently available sea surface temperature were assumed to be higher, nonmarine clouds and were removed from the computations. The results presented represent the computed hourly mean percent albedo.

Evaluations were made of using the infrared band to extend the cloud observations into the nighttime. Comparing remotely sensed temperatures in clear and cloudy skies with buoy temperatures shows this technique to be satisfactory.

3. Wind and divergence fields

To investigate the longer-term (monthly) significance of local maxima and their diurnal trends, we analyzed MM5 hourly simulations for all of June 1996. Figure 6 shows a nighttime [0200 local standard time (LST)] wind vector plot overlaid with isolines of the simulated monthly averages of wind speed at the level closest to the surface (approximately equal to 20 m AGL). The flow exhibits isolated wind speed maxima in excess of 10 m s^{-1} downwind of Cape Blanco, Cape Mendocino, Point Arena, Point Sur, and Point Conception. By the early afternoon (1400 LST), there is a significant change in the monthly averaged near-coast flow field (Fig. 7). A maximum wind speed is simulated in the lee of every major cape. Paired with each maximum is an upstream minimum. We investigated this effect further by comparing the monthly averaged diurnal trend of the *U* and *V* wind components in one of the compression bulges (Fort Bragg), one of the expansion fans (Point Arena), and a deceleration area (San Francisco) (Fig. 8). There is a significant increase in both *U* and *V* wind components during the daytime. Although the main increase in the alongshore wind component is induced by the coastal baroclinity, the results shown in Fig. 8 indicate that the daytime mesoscale pressure gradient directed onshore increases, as does the *U* component and the resultant alongshore component. The diurnal trend of the *U* and *V* components in the compression bulges shows a similar trend, but with a smaller increase.

Figures 9a and 10a show the calculated divergence of the simulated flow field. The greatest late night divergence field is within 100 km of the coast, while there is little beyond the coastal region (Fig. 9a, 0200 LST). In the early afternoon (Fig. 10a, 1400 LST), the surface divergence increases in the inner coastal zone, so that a sequence of isolated downstream maxima (expansion fan areas) and upstream minima (compression bulges) are simultaneously matched in the surface wind pattern. The detailed structure of the compression bulge and expansion fan around Point Arena is shown in Figs. 9b and 10b. This structure is typical of all major coastal points. During the nighttime, the expansion fans generally cover an area similar to that of the compression bulges. During the daytime, each cape has a large expansion fan downwind and a smaller, weaker compression bulge upwind. Near sea level, divergence is greatest in the early afternoon, and diurnal effects rapidly decrease offshore. Figures 9 and 10, in particular Figs. 9b

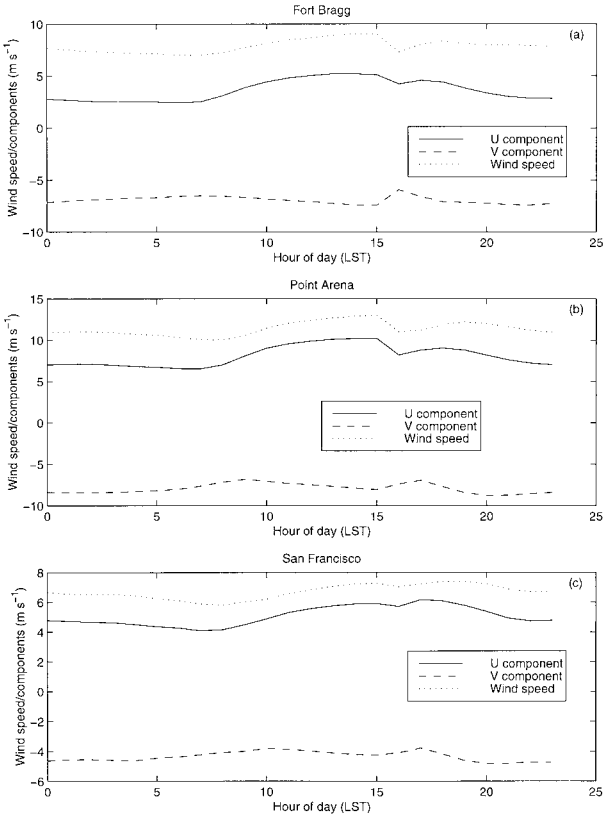

FIG. 8. Diurnal trends of simulated wind components and wind speed at 20 m AGL averaged by hour for all of Jun 1996. Locations, as marked in Fig. 1, are off Fort Bragg (B), Point Arena (A), and San Francisco (S).

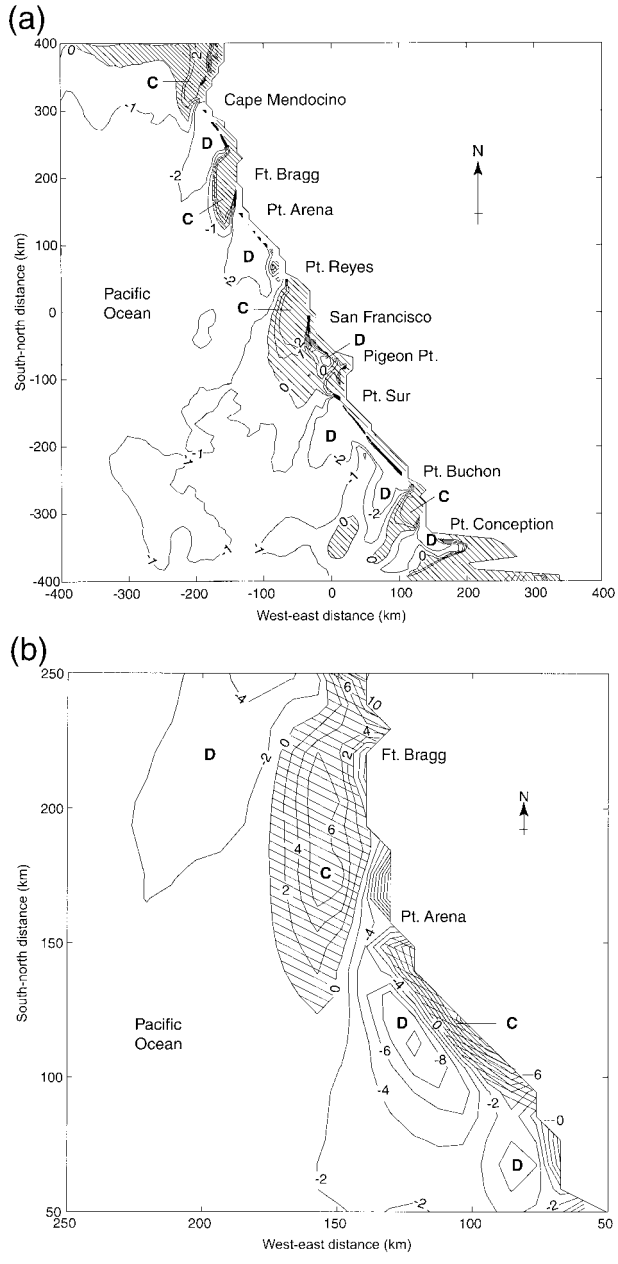

FIG. 9. (a) Simulated wind convergence (positive values hatched, centers marked by C) and divergence (negative values, centers marked by D) at 20 m AGL averaged for 0200 LST for all of Jun 1996. Contour interval is 1×10^{-5} s^{-1}. (b) Enlargement of the area around Point Arena in (a). Contour interval is 2×10^{-5} s^{-1}.

and 10b, show that in the lees of the major capes there is a narrow convergence zone between the edge of the expansion fan and the coastline. The formation of this convergence zone is due to the channeling of the expansion fan flow while approaching coastal topography; consequently, this effect is not present at the offshore edge of the expansion fan.

The daytime heating and associated increase in the cross-shore pressure gradient induces low-level baroclinity. As a result of geostrophic adjustment, the alongshore wind speed increases and alters the divergence field. Variation in alongshore topography then modifies the final inhomogeneous structure of the divergence field. Diurnal variability of baroclinity induces diurnal variability in the divergence field. The strongest divergence occurs during the daytime, when the contrast between the shallow marine layer and the deep inland boundary layer is greatest. Figure 11a shows a diurnal variation based on the month-long, hourly model results of the flow divergence simulated in the expansion fan downwind of Point Arena, which is always divergent. A pronounced daytime extreme results as a response to the strong baroclinity. The general relationship between the strong divergence at the surface and the weak convergence at 1564 m AGL is also evident in the time series for all of June 1996 (Fig. 12). In most of the cases, larger surface divergence is associated with larger convergence at the higher levels. Figure 11b shows the diurnal variation of the surface divergence field off Point Arena as simulated in the region of the largest divergence in the expansion fan and also at locations in 45-km increments west of the expansion fan. The significant divergence field and its diurnal trend are dominant only near the coast.

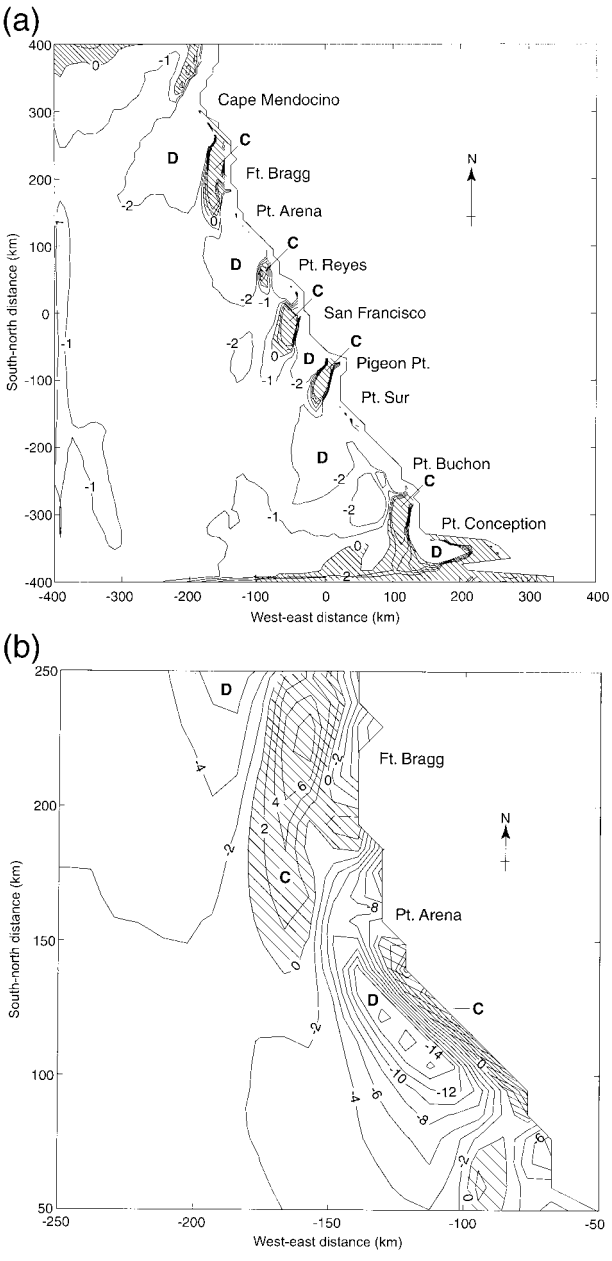

FIG. 10. (a) Simulated wind convergence (positive values hatched, centers marked by C) and divergence (negative values, centers marked by D) at 20 m AGL averaged for 1400 LST for all of Jun 1996. Contour interval is 1×10^{-5} s^{-1}. (b) Enlargement of the area around Point Arena in (a). Contour interval is 2×10^{-5} s^{-1}.

The MABL flow decelerates upwind of an obstacle and downwind from the expansion fan. The compression bulge upwind of Point Arena is near Fort Bragg (Fig. 13a), while the next large compression area is off San Francisco (Fig. 14a). The diurnal convergence trend off San Francisco shares the general characteristics of the compression bulge upwind of Point Arena even though there is a large gap in the coastal mountains that might allow divergent flow into the Bay Area and the central

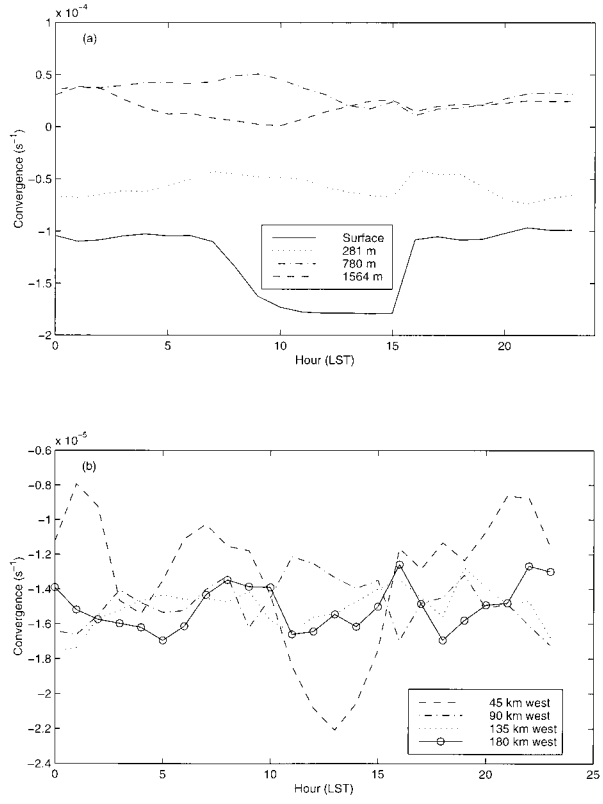

FIG. 11. Diurnal trend of simulated model convergence at (a) surface (20 m), 281, 780, and 1564 m AGL in the lee of Point Arena; and (b) at 20 m AGL, at 45 km intervals west of the lee of Point Arena.

valley of California beyond. In contrast to the expansion fans, the compression bulges are convergent at night and display weak divergence around noon. The surface divergence/convergence is strongest near the coast and

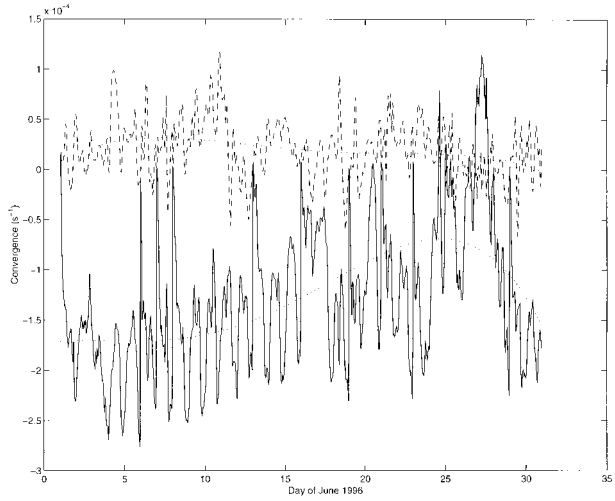

FIG. 12. Time series of simulated convergence near the surface (20 m AGL, solid line) and at 1564 m AGL (dashed line) in the lee of Point Arena for all of Jun 1996.

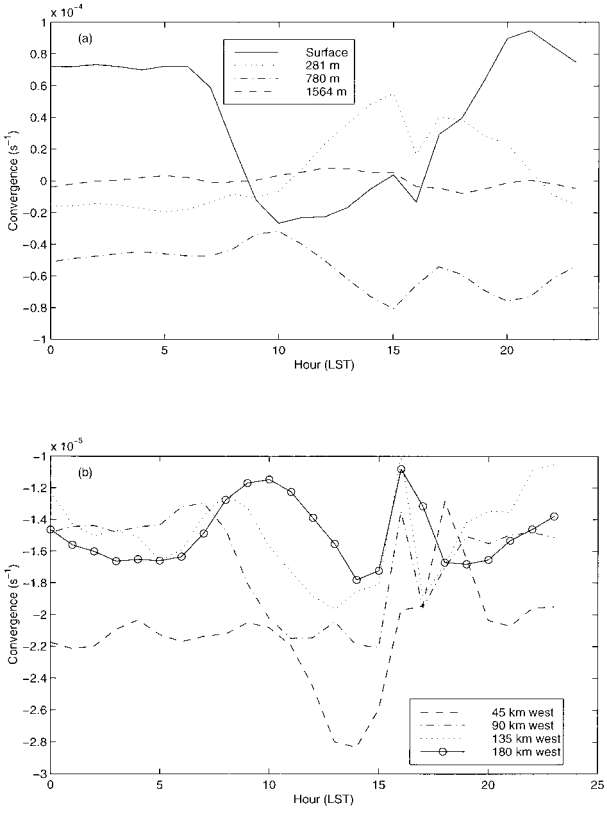

FIG. 13. Diurnal trend of simulated convergence off Fort Bragg (a) near the coast at 20, 281, 780, and 1564 m AGL; and (b) in 45-km intervals west of Fort Bragg at 20 m AGL.

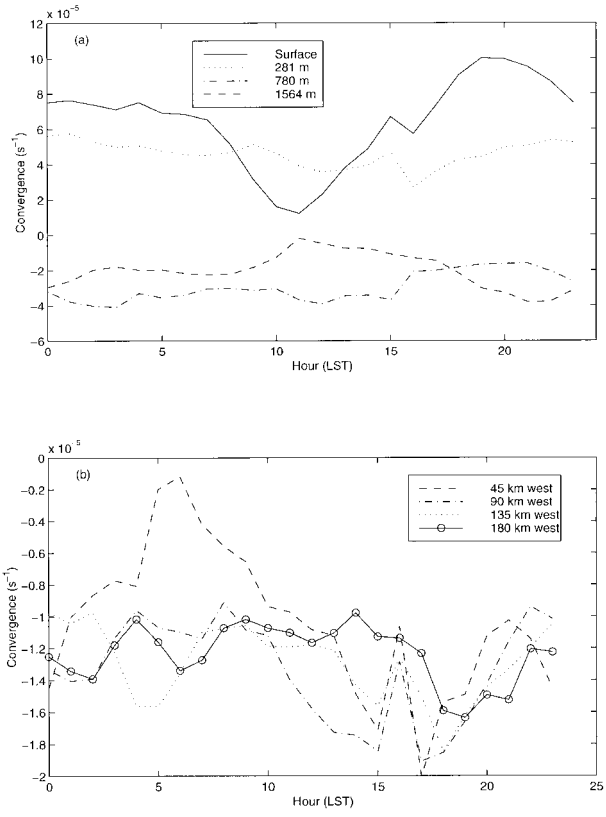

FIG. 14. Diurnal trend of simulated convergence off San Francisco (a) near the coast at 20, 281, 780, and 1564 m AGL; and (b) in 45-km intervals west of San Francisco at 20 m AGL.

rapidly decreases in magnitude offshore (Figs. 11b, 13b, and 14b).

The Cape Mendocino expansion fan diurnal trend is also presented since this cape extends farther outward than any other on the west coast (Fig. 15). It marks a climatic boundary, with substantially faster surface winds to the south than to the north (Dorman and Winant 1995). It also has the largest, most dependable compression bulge cloud (visible in Fig. 24), which tends to be greatest in horizontal extent at sunrise and least in the afternoon; however, this cloud appears similar to the one upwind of the topographically smaller cape at Point Arena (Fig. 11). Vertical profiles of monthly averaged wind divergence for typical daytime (1400 LST) and nighttime (0200 LST) hours indicate several interesting features (figure not shown). In both cases the surface divergence reverses to convergence between 300 and 400 m AGL; however, the daytime near-surface divergence is greater than the nighttime one and remains nearly constant with height within the MABL. The nighttime divergence is greatest near the surface and decreases almost linearly with height. The compensating convergence field is also varying diurnally above 400 m up to approximately 1000–1200 m AGL.

Since the general nature of the diurnal divergence variation around the other four major capes along the California–Oregon coast is similar to that around Point Arena, they are not shown.

4. MABL depth and Froude number

a. Depth of the marine atmospheric boundary layer

The top of the MABL, closely related to the MABL divergence and supercriticality, is computed as the bottom of the layer below 1500 m AGL that has the largest potential temperature gradient. In order to further evaluate MM5's capability in reproducing the stability and structure of the MABL, we compared estimates of MABL depth from both the model results and radiosonde data at Oakland (37.75°N, 122.22°E). Figure 16 shows a time series of simulated and measurement-derived MABL depth. The model agrees closely with the measurements, and the overall correlation coefficient is 0.73. Although there is uncertainty related to the limitations in vertical resolution for both the measurements and the model, the trend of the increase and decrease in MABL depth is also well reproduced by the model.

The offshore distribution of MABL depth for 0200 LST, determined from the monthly averaged temperature field, is shown in Fig. 17. There is a maximum upwind and a minimum downwind in MABL depth at

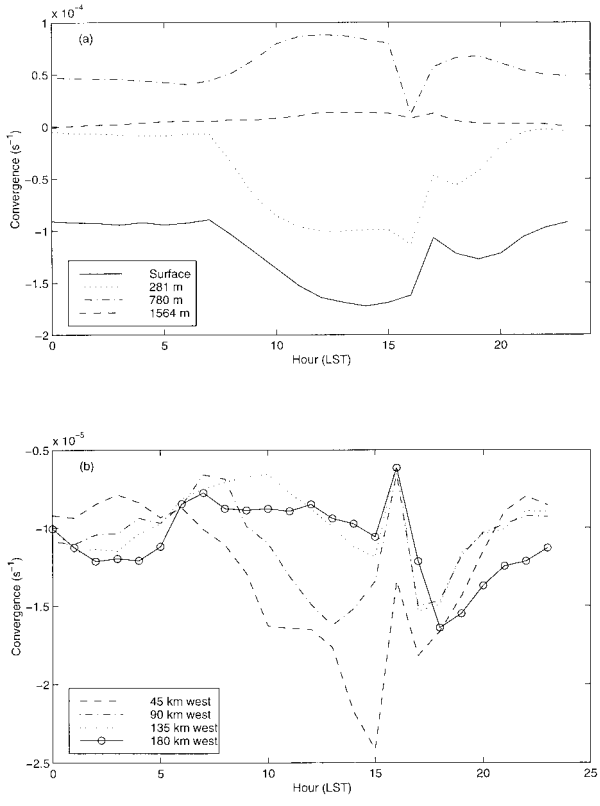

FIG. 15. Diurnal trend of simulated convergence off Cape Mendocino (a) near the coast at 20, 281, 780, and 1564 m AGL; and (b) in 45-km intervals west of Cape Mendocino at 20 m AGL.

each of the five major capes. With the exception of the areas near San Francisco and Monterey Bay, the depth is generally less than 350 m near the coast. At distances beyond 100–200 km offshore, the depth rapidly increases to more than 450 m. At 1400 LST, the MABL

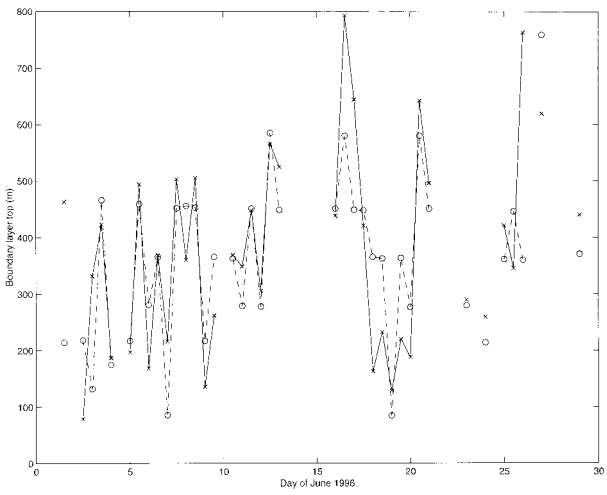

FIG. 16. Time series of the boundary layer top (m) as computed from the MM5 model results (dashed line O) and radiosonde data (solid line X) at Oakland, CA, for all of Jun 1996.

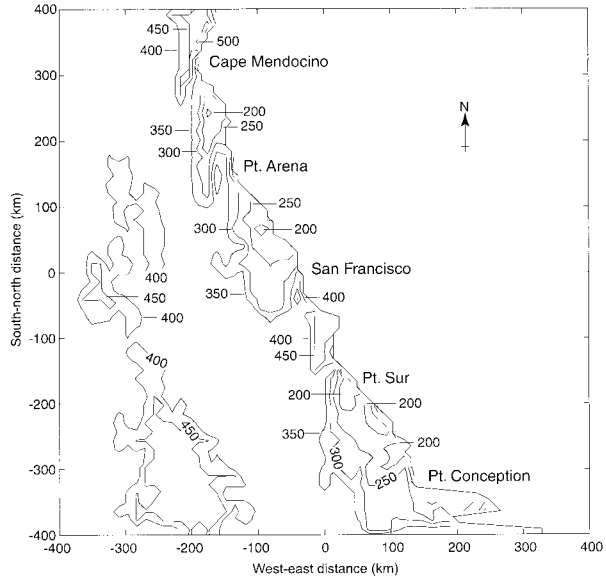

FIG. 17. Simulated MABL depth (m) for 0200 LST averaged for all of Jun 1996. Contour interval is 50 m.

depth is less than that at 0200 LST everywhere, with the greatest changes occurring near the shore (Figs. 17 and 18). Around 100 km in the offshore direction, the average MABL depth rises quickly from 300 to 350 m and then increases more slowly farther offshore. The greatest changes in the MABL depth are in the expansion fans. Among the compression bulges, the greatest decline in MABL depth is off San Francisco.

A near-coast sloping inversion and dynamically driven modification of the MABL depth influence the average vertical thermal stability within the marine layer.

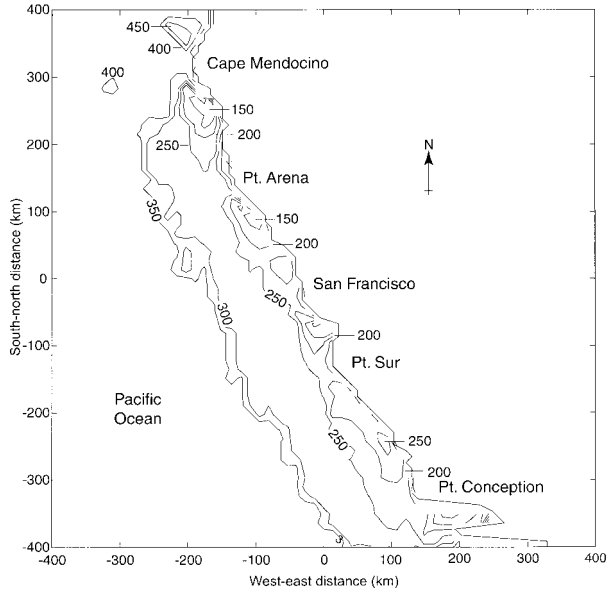

FIG. 18. Simulated MABL depth (m) for 1400 LST averaged for all of Jun 1996. Contour interval is 50 m.

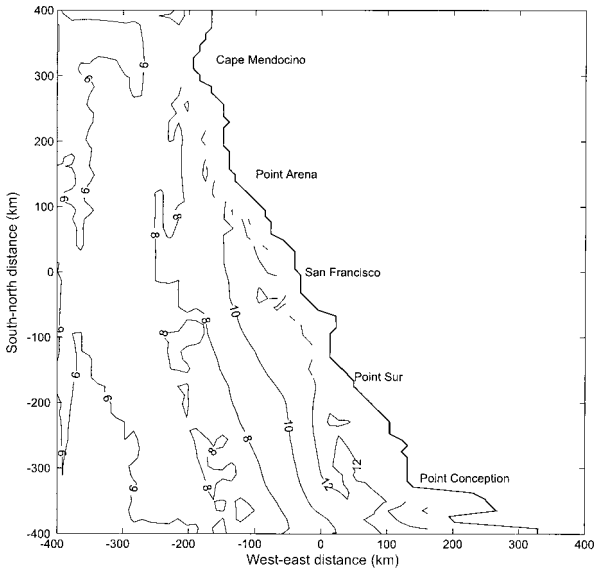

FIG. 19. Marine layer stability (K km^{-1}) as simulated by the MM5 model for all of Jun 1996 averaged for 0200 LST. Contour interval is 2 K km^{-1}.

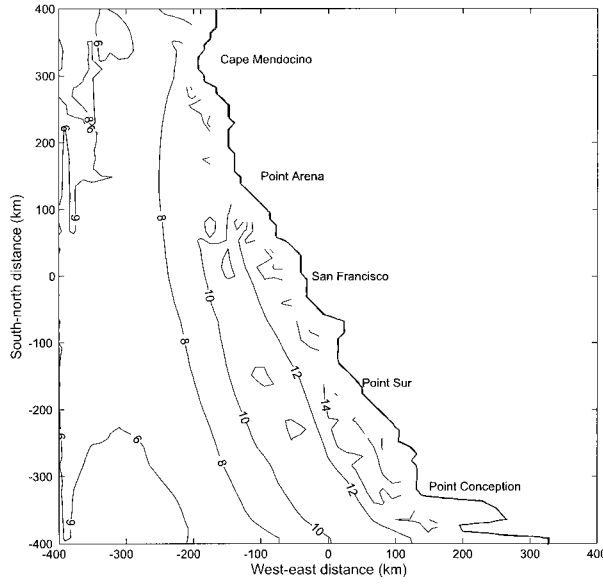

FIG. 20. Marine layer stability (K km^{-1}) as simulated by the MM5 model for all of Jun 1996 averaged for 1400 LST. Contour interval is 2 K km^{-1}.

Average vertical thermal stability was calculated as the gradient of the potential temperature between the inversion top and the lowest model level. Figures 19 and 20 show the spatial distribution of the vertical potential temperature gradient for nighttime and daytime hours, respectively. A shallow marine layer is associated with a greater potential temperature gradient, while a deeper marine layer is characterized by a weaker temperature gradient. The zone of stable conditions extends approximately 100 km offshore in the northern part and more than 200 km offshore in the southern part of the California coast. During the day, the stability is generally stronger than during the night and is significantly greater (14–16 K km^{-1}) in the expansion fans in the lees of Point Arena and Point Sur. In general, a decrease in the MABL depth from 300 to 200 m will cause an increase in the potential temperature gradient of about 1.5 K km^{-1}. This will have a significant impact on the estimate of flow supercriticality, as will be shown in section 4c.

b. Entrainment

According to the model results, the dynamically enhanced, low-level divergence due to wind has relatively large absolute value, usually with values in the expansion fans of -10^{-5} s^{-1} or less. Consequently, it is important to estimate the variation in the MABL top related to dynamically enhanced subsidence and entrainment. We assume that diurnal variation in the MABL top can be represented by diurnal variation in the characteristic divergence fields within the MABL. Knowing the diurnal variation of the modeled MABL top and wind divergence field, the associated diurnal variation of entrainment at the MABL top can be estimated. Assuming that the rate of change in the MABL top (h) is determined by entrainment and dynamically enhanced subsidence within the MABL (see the significance of the latter in Fig. 12), the entrainment rate (w_e) can be expressed as

$$w_e = \frac{\Delta h}{\Delta t} - w_d, \tag{5}$$

where w_d is the MABL dynamically enhanced subsidence rate, and h is the height of the MABL top. We determined the monthly averaged 3D divergence fields for each hour of the day and selected the lee of Cape Mendocino as an example. We calculated the daytime average divergence between 0700 and 1900 LST and the nighttime for the remaining hours, both below 300 m. As expected, the daytime average divergence was greater in magnitude (-1.235×10^{-4} s^{-1}) than the nighttime average (-0.585×10^{-4} s^{-1}). Assuming constant average divergence and a linear subsidence profile within 300 m, the daytime average subsidence is -3.7 cm s^{-1} and the nighttime average is -1.8 cm s^{-1} at the MABL top. The model results suggest that the MABL top decreased by about 50 m during the daytime and rose by 50 m during the nighttime. We assume that this change occurs within 12 h. Using the simplified entrainment formula above, the average corresponding entrainment rate appears to be 3.6 cm s^{-1} during the daytime and 1.9 cm s^{-1} during the nighttime. Consequently, using this simplistic approach, the diurnal variation in the MABL top and wind divergence appears to induce the diurnal variation of entrainment at the MABL top. These entrainment rates are generally overestimated since the advective component of the rate of change in

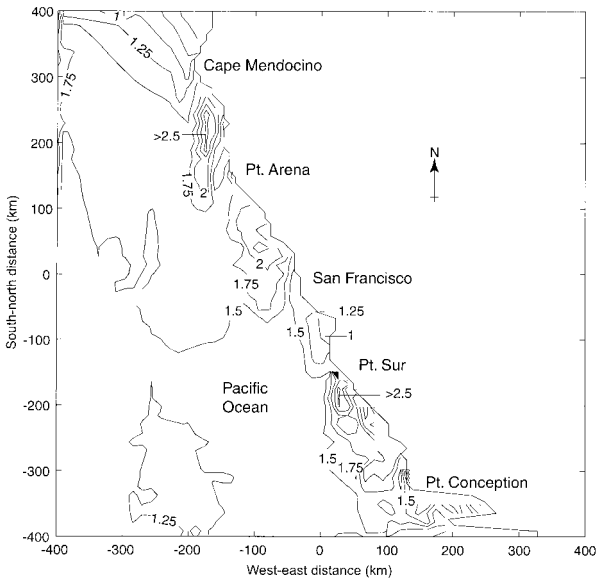

FIG. 21. Froude number estimated from the MM5 results for 0200 LST averaged for all of Jun 1996. Contour interval is 0.25.

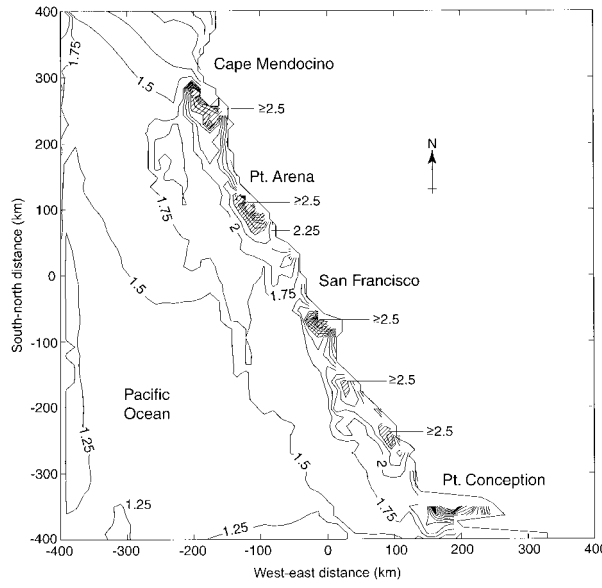

FIG. 22. Froude number estimated from the MM5 results for 1400 LST averaged for all of Jun 1996. Contour interval is 0.25.

the MABL top was not considered (Lenshow 1973; Stull 1997). As evidenced from contours of the MABL top in Figs. 17 and 18, the advective components appear to be significant in understanding the evolution of the MABL in the lees of the capes. The contribution to the entrainment rate due to the advection ($w_{e(\mathrm{adv})}$) of the deeper MABL from the north and west can be estimated as

$$w_{e(\mathrm{adv})} = U\frac{\Delta h}{\Delta x} + V\frac{\Delta h}{\Delta y}. \tag{6}$$

Therefore, the final expression for the entrainment rate is

$$w_e = \frac{\Delta h}{\Delta t} + U\frac{\Delta h}{\Delta x} + V\frac{\Delta h}{\Delta y} - w_d. \tag{7}$$

Taking typical values of the MABL top at locations 50–70 km to the north and to the west of Cape Mendocino, and corresponding averaged U and V wind components for nighttime and daytime hours, the advective component appears to be of opposite sign and similar magnitude to the dynamically induced subsidence for nighttime and daytime, respectively. Consequently, the average entrainment rate is of similar magnitude (0.6 cm s^{-1}) for nighttime and daytime.

c. Supercriticality of the flow

The Froude number (Fr), expressed as the ratio of the inertial and buoyancy effects, is a measure of flow regime and its properties with respect to the propagation of gravity wave perturbations. The Fr is calculated as

$$\mathrm{Fr} = \frac{U}{hN}, \tag{8}$$

where U is the characteristic wind speed, h is the MABL depth, and N is the Brunt–Väisälä frequency. The characteristic wind speed U is chosen as the mean wind speed at the top of the MABL, and the Brunt–Väisälä frequency is calculated at the inversion base.

The Froude number calculated from the monthly average parameters for the entire offshore region is greater than one for both the early morning (Fig. 21) and afternoon (Fig. 22) hours. Most of the change from early morning to afternoon is in the along- and cross-shore MABL structures within about 100 km of the coast. Downwind of each major cape is an Fr maximum that corresponds to an area of high winds and shallow MABL. Upwind of each major cape is an Fr minimum that corresponds to lower winds and deeper MABL. In the offshore direction, Fr decreases due to lower wind speeds and deeper MABL. Although Fr incorporates uncertainty in the somewhat arbitrary way of determining U and N within the layered MABL structure, these results indicate that the flow on the West Coast is expected to be supercritical on rather long timescales and large spatial scales during the warm season. Simulation results and estimated supercriticality downwind of Cape Mendocino and Point Sur resemble the patterns observed by aircraft (Rogers et al. 1998).

Figure 23 illustrates the differences in occurrence of flow supercriticality during the entire month in the Point Arena expansion fan and its upwind (Fort Bragg) and downwind (San Francisco) regions. The flow is dominantly supercritical in all of these locations during the entire month (73% of all hours). The percentage of occurrence is higher in the expansion fan (86% of all hours) and lower in the upwind (61%) and downwind (71%) areas. The flow in the upwind and downwind

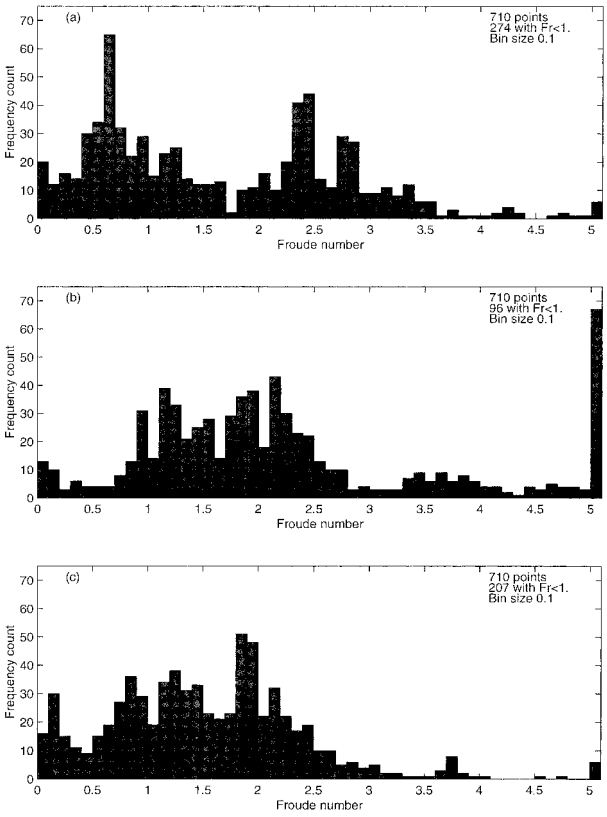

FIG. 23. Froude number frequency of occurrence estimated from the MM5 results (a) upwind of Point Arena (Fort Bragg), (b) downwind of Point Arena, and (c) off San Francisco. Bin size is 0.1.

areas is frequently transcritical ($0.5 < \mathrm{Fr} < 1$). Rogerson (1999) showed that an expansion fan can form in the lee of a major cape during these transcritical flow conditions.

5. Clouds

Satellite cloud images are useful for inferring the MABL structure, as the marine cloud cover tends to be proportional to the MABL depth (Dorman et al. 2000). Stationary satellite images in the visible band at 15-min intervals with a resolution of about 1 km are of a scale similar to the model resolution and cover the same domain; thus, they may be used as observational evidence of the approximate horizontal MABL structure. Since images in the visible band are taken during daylight only, the average June 1996 percent albedo at 0730–0830 LST and at 1330–1430 LST are shown to provide a sense of diurnal change (Figs. 24, 25). The albedo is at a maximum in the early morning (Fig. 24), and there is a general trend toward higher albedo to the south, with the greatest values in the Southern California Bight. In the first 100 km off the coast, there is substantial horizontal structure, with local maxima associated with coastal topographic features. There is a minimum in the lee of each cape that covers an area roughly

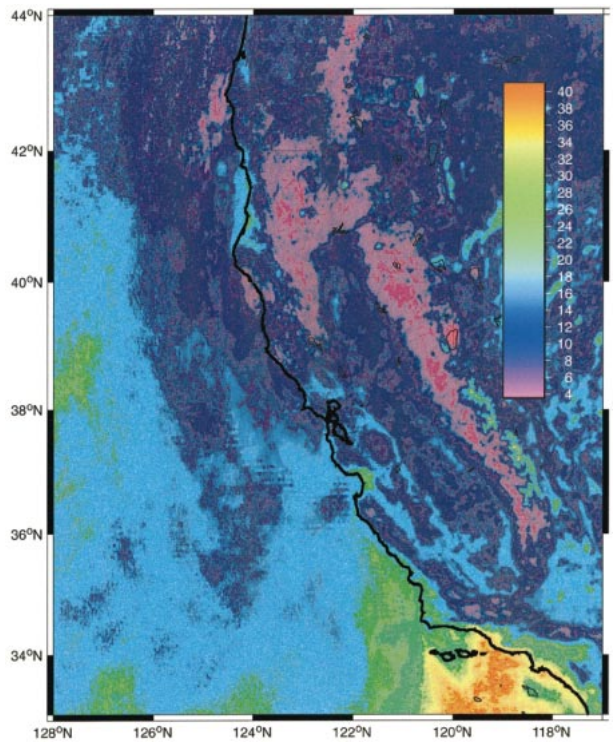

FIG. 24. Stationary satellite measured cloud albedo (%) averaged for 0800 LST for all of Jun 1996.

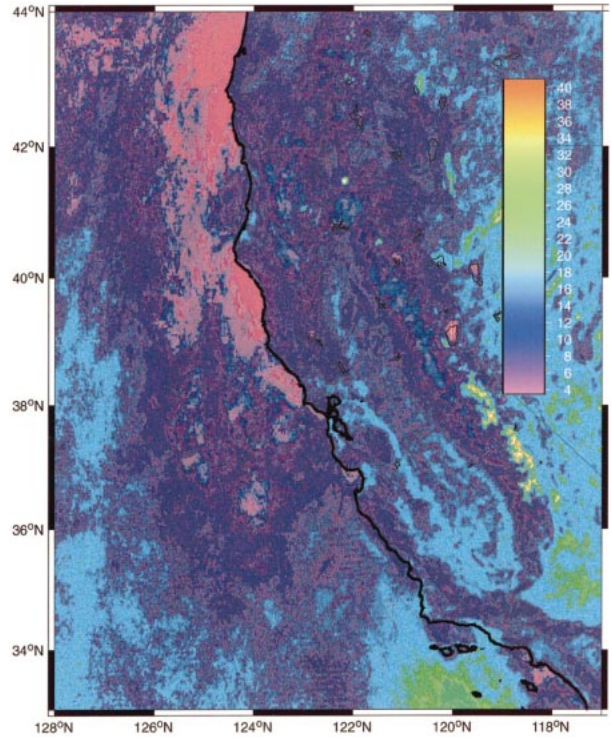

FIG. 25. Stationary satellite measured cloud albedo (%) averaged for 1200 LST for all of Jun 1996.

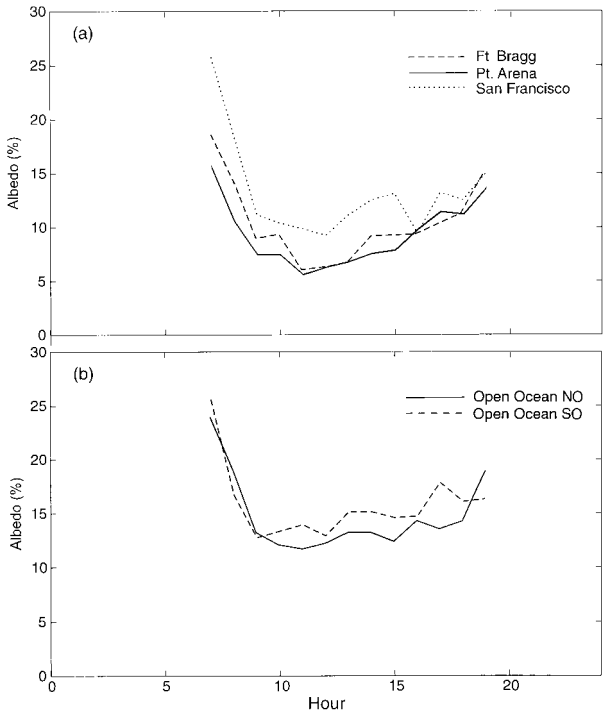

FIG. 26. Diurnal trend of satellite-derived albedo (%) for (a) upwind of Point Arena (Fort Bragg, site B), in the lee of Point Arena (site A), and off San Francisco (site S); and (b) the north offshore (site NO) and the south offshore (site SO). The sites are shown in Fig. 1.

proportional to the size of the cape, so that it is larger for larger capes such as Cape Blanco, Cape Mendocino, and Point Conception; intermediate for intermediate-sized capes such as Point Arena; and smaller for smaller capes such as Pigeon Point and Point Buchon. A minimum in the cloud area in the lee of Point Sur cannot be distinguished until a couple of hours later in the day, which may be related to the thickness of the cloud in the area, or it may be that the width of any minimum is too narrow to be distinguished. In the afternoon (Fig. 25), the albedo at all locations is reduced, with greater clearing at latitudes north of San Francisco than south. In addition, there is relatively greater clearing in the lees of the capes and weaker clearing on the upwind sides of capes.

Figure 26a shows the diurnal trend in the daylight albedo for a point upwind of Point Arena, in the lee of Point Arena, and in the deceleration area. A similar trend in albedo is observed at the other capes. In all cases the cloud cover decreases sharply in the morning from sunrise to 0900–1000 LST. The leeside albedo does not significantly change until 1600 LST. The albedo at the upwind and far downwind sites increases slowly from noon until sunset.

Nighttime infrared GOES observations support the inference from the visible band observations in the early morning and afternoon that marine clouds grow at night. As noted in section 2, the difference in the buoy temperature and GOES channel 4 (infrared) temperature was computed for five west coast National Data Buoy Center buoys. Although very noisy, the data show that this difference tends to increase slowly from sunset to sunrise. The near-shore diurnal trends shown in the satellite visible band, extended by the infrared band, are consistent with the simulated divergence field. The simulated divergence has a broad minimum at night and rapidly changes to a maximum in divergence around noon.

As with the near-shore observations, there is a significant diurnal trend in the albedo at offshore locations (Fig. 26b, areas NO and SO). This is in contrast to the simulated surface divergence, which is weak and does not have a clear diurnal trend (Figs. 9a and 10a). This suggests that cloud radiative effects dominate the diurnal variability observed offshore. Such diurnal trends in cloud radiation processes have been observed in the field (Nicholls 1984) and are supported by model studies (Koračin and Rogers 1990; Rogers and Koračin 1992; Tjernström and Koračin 1995). It should be noted that although the clouds albedo exhibits weaker diurnal variation over the open ocean than in the near-shore zone, its values are smaller in the near-shore zone due to the dynamically-enhanced subsidence (minimum only about 5%, Fig. 26b) than in the open ocean regions (minimum about 10%, Fig. 26b).

Other studies have confirmed the occurrence of an early afternoon minimum in cloudiness along the California coast (Betts 1990; Blaskovic et al. 1991). Aircraft measurements (Beardsley et al. 1987; Dorman et al. 1999, 2000) also show that the MABL thins toward the coast, eastward of the cloud maximum.

6. Summary and conclusions

Based on month-long, hourly mesoscale simulations and observations, this study lends support to the important role of diurnal effects on MABL dynamics and cloudiness along the California coast. Specific results include the following.

- The spatial structure of divergence fields from the northern to the southern California coast and to 300 km offshore has been simulated by the MM5 model. The coast from Cape Mendocino to Point Conception is covered by alternating pairs of compression bulges (convergent flow) and expansion fans (divergent flow).
- The divergent flow in the expansion fans and the convergent flow in both the compression bulges and the deceleration areas exhibit a diurnal trend.
- During the daytime, the region of divergent flow, as compared to convergent flow, has a greater absolute value of divergence, extends farther offshore, and covers a larger area.
- In the first 100 km off the coast (the inner coastal zone), the MABL structure (flow, stability, Fr number,

and observed cloudiness) is governed by topographically induced features such as compression bulges, expansion fans, and deceleration regions.
- Diurnal variation (in the winds, divergence, MABL depth, atmospheric stability, Fr number, and observed cloudiness) is greatest in the inner coastal zone.
- The divergence field is at maximum at the surface and rapidly decreases with height as well as in the offshore direction; the diurnal variation of divergence becomes small beyond the inner coastal zone.
- The divergence field has a significant role in determining marine layer cloudiness in the near-shore zone. The cloud albedo is smaller and its diurnal variation is more pronounced in the near-shore zone as compared to the open-ocean regions.
- The cloudiness variation in the far offshore zone (beyond 100 km) is mainly due to cloud radiative effects.

Since simulation of cloudiness has uncertainties and errors due to input parameters, limitations of parameterization schemes, and even problems in determining ways to evaluate model results, we extended the usual model evaluation in the temporal–spatial and spectral domains by investigating causality between the evaluated model's dynamics and satellite-derived cloudiness. This approach contributes to another level of evaluating the model's dynamics using satellite data.

The results from this study constitute an initial effort to understand the month-long, offshore mesoscale processes along the U.S. West Coast by focusing on the diurnal effects of the MABL dynamics and cloudiness.

Acknowledgments. This study was supported by the Department of Defense, Office of Naval Research, Marine Meteorology and Atmospheric Effects, Grants N00014-94-1-0232, N00014-96-1-0980, N00014-96-1-1235, and N00014-00-1-0524. The authors are grateful to Dr. Joost A. Businger of the University of Washington, Dr. Dale Leipper of the Desert Research Institute (DRI), Dr. John Lewis (DRI and NOAA), and Dr. Jordan Powers if the National Center for Atmospheric Research, Boulder, Colorado, for valuable discussions, comments, and encouragement in conducting the study. Thanks to Dr. Vlad Isakov (formerly at DRI and presently at California Air Resources Board, Sacramento), Mr. Domagoj Podnar (DRI), and Mr. Travis McCord (DRI) for technical preparation of the manuscript. Mr. Roger Kreidberg (DRI) is acknowledged for editorial assistance.

REFERENCES

Beardsley, R. C., C. E. Dorman, C. A. Friehe, L. K. Rosenfeld, and C. D. Winant, 1987: Local atmospheric forcing during the Coastal Ocean Dynamics Experiment: A description of the marine boundary layer and atmospheric conditions over a Northern California upwelling region. *J. Geophys. Res.,* **92,** 1467–1488.

Betts, A. K., 1990: Diurnal variation of California coastal stratocumulus from two days of boundary layer soundings. *Tellus,* **42A,** 302–304.

Blackadar, A. K., 1979: High resolution models of the planetary boundary layer. *Advances in Environmental Sciences and Engineering,* J. R. Pfafflin and E. N. Ziegler, Eds., Vol. 1, Gordon and Breach, 50–81.

Blaskovic, M., R. Davies, and J. B. Snider, 1991: Diurnal variation of marine stratocumulus over San Nicolas Island during July 1987. *Mon. Wea. Rev.,* **119,** 1469–1478.

Burk, S. D., and W. T. Thompson, 1996: The summertime low-level jet and marine boundary layer structure along the California coast. *Mon. Wea. Rev.,* **124,** 668–686.

Dorman, C. E., 1985: Hydraulic control of the northern California marine layer (abstract). *Eos, Trans. Amer. Geophys. Union,* **66,** 914.

——, and C. D. Winant, 1995: Buoy observations of the atmosphere along the west coast of the United States. *J. Geophys. Res.,* **100,** 16 029–16 044.

——, and ——, 2000: The structure and variability of the marine atmosphere around the Santa Barbara Channel. *Mon. Wea. Rev.,* **128,** 261–282.

——, D. P. Rogers, W. A. Nuss, and W. T. Thompson, 1999: Adjustment of the summer marine boundary layer around Point Sur, California. *Mon. Wea. Rev.,* **127,** 2143–2159.

——, T. Holt, D. P. Rogers and K. Edwards, 2000: Large-scale structure of the June–July 1996 marine boundary layer along California and Oregon. *Mon. Wea. Rev.,* **128,** 1632–1652.

Grell, G. A., J. Dudhia, and D. R. Stauffer, 1995: A description of the fifth-generation Penn State/NCAR Mesoscale Model (MM5). National Center for Atmospheric Research Tech. Note TN-398, 122 pp.

Koračin, D., and D. P. Rogers, 1990: Numerical simulations of the response of the marine atmosphere to ocean forcing. *J. Atmos. Sci.* **47,** 592–611.

——, and M. Tjernström, 1992: Impact of clouds on a boundary layer structure. Preprints, *Tenth Symp. on Turbulence and Diffusion,* Portland, OR, Amer. Meteor. Soc., 19–21.

——, J. Frye, V. Isakov, and P. Saha, 1997: Observations and simulations of the coastal jet during the Coastal Waves Program in June 1996. *Proc. 12th Symp. on Boundary Layers and Turbulence,* Vancouver, BC, Canada, Amer. Meteor. Soc., 352–353.

——, V. Isakov, and D. F. Leipper, 1998: Simulations of the sea breezes on the central U.S. California coast. *Hydraulic Engineering Software,* W. R. Blain, Ed., Wessex Institute of Technology Press, 307–316.

Lenschow, D. H., 1973: Two examples of planetary boundary layer modification over the Great Lakes. *J. Atmos. Sci.,* **30,** 568–581.

Neiburger, M., D. S. Johnson, and C. W. Chien, 1961: *The Inversion over the Eastern North Pacific Ocean.* Vol. 1, *Studies of the Structure of the Atmosphere over the Eastern Pacific in Summer,* University of California Press, 58 pp.

Nelson, C. S., 1977: Wind stress curl over the California current. NOAA Tech. Rep. NMFS SSRF-714, 87 pp.

——, and D. M. Husby, 1983: Climatology of surface heat fluxes over the California current region. NOAA Tech. Rep. NMFS SSRF-763, 155 pp.

Nicholls, S., 1984: The dynamics of stratocumulus: Aircraft observations and comparison with a mixed layer model. *Quart. J. Roy. Meteor. Soc.,* **110,** 783–820.

Rogers, D. P., and D. Koračin, 1992: Radiative transfer and turbulence in the cloud-topped marine atmospheric boundary layer. *J. Atmos. Sci.,* **49,** 1473–1486.

——, and Coauthors,1998: Highlights of Coastal Waves 1996. *Bull. Amer. Meteor. Soc.,* **79,** 1307–1326.

Rogerson, A. M., 1999: Transcritical flows in the coastal marine atmospheric boundary layer. *J. Atmos. Sci.,* **56,** 2761–2779.

Samelson, R. M., 1992: Supercritical marine-layer flow along a smoothly varying coastline. *J. Atmos. Sci.,* **49,** 1571–1584.

Stull, R. B., 1997: *An Introduction to Boundary Layer Meteorology.* Kluwer Academic, 670 pp.

Sundararajan, R., and M. Tjernström, 2000: Observations and sim-

ulations of a non-stationary coastal atmospheric boundary layer. *Quart. J. Roy. Meteor. Soc.,* **126,** 445–476.
Tjernström, M., 1999: Sensitivity of coastal atmospheric supercritical flow to ambient conditions. *Tellus,* **55,** 880–901.
——, and D. Koračin, 1995: Modeling the impact of marine stratocumulus on the boundary-layer structure. *J. Atmos. Sci.,* **52,** 863–878.
——, and B. Grisogono, 2000: Simulations of supercritical flow around points and capes in the coastal atmosphere. *J. Atmos. Sci.,* **57,** 108–135.
Winant, C. D., C. E. Dorman, C. A. Friehe, and R. C. Beardsley, 1988: The marine layer off Northern California: An example of supercritical channel flow. *J. Atmos. Sci.,* **45,** 3588–3605.